PNAS RESEARCH ARTICLE | EARTH, ATMOSPHERIC, AND PLANETARY SCIENCES
ECOLOGY OPEN ACCESS

Depth of nutrient uptake by deep-rooted plants is regulated by water availability

Langlang Li[a,b], John N. Christensen[b], Markus Bill[b], Wenming Dong[b], Yuxin Wu[b], Curtis Beutler[b,c], Matthias Sprenger[b,d], Brian W. Gulick[e], Sharon E. Bone[f], Boris Faybishenko[b], John Sanders[g], Chunwei Chou[b], Amanda Henderson[c], Nicholas J. Bouskill[b,h], Kenneth H. Williams[b,c], and Benjamin Gilbert[a,b,1]

Affiliations are included on p. 6.

Edited by Joel D. Blum, University of Michigan, Ann Arbor, MI; received October 9, 2025; accepted February 11, 2026

The capacity of some plants to access water and nutrients at depths greater than one meter is a critical functional trait that confers resistance to drought and impacts both belowground and shallow soil processes. Here, we report water and strontium isotopic data from an alpine meadow transect showing the correlation between water and nutrient acquisition depths. The isotopic compositions of Sr ($^{87}Sr/^{86}Sr$ ratio) and water in rock and soil, and in plant leaf tissues, reveal that deeper-rooted plants acquire a higher proportion of water, Sr, and cation nutrients that are derived from the saprolite, a zone of silicate weathering, than shallow-rooted grass. A three-decade dendrochemical record reveals that reductions of wet precipitation drive deep-rooted plants to acquire cation nutrients from deeper saprolite or bedrock regions. Thus, the depth of cation nutrient acquisition by deep-rooted plant species at this site is tightly coupled with, and likely determined by, water availability in soil, saprolite, and bedrock. The enhanced uptake of cations as well as water from deeper saprolite zones could impact the rate of bedrock weathering and watershed chemistry during drought.

deep root | drought resilience | mineral weathering | biogeochemistry | strontium isotopes

Significance

Plant uptake of water and nutrients occurs mostly in soil top layers. Some plants with deep roots can also obtain water from deeper regions in the saprolite, the boundary between soil and bedrock. Deep water uptake can provide resistance to drought for those plants and their surrounding ecosystem. Here, we provide evidence that when deep-rooted plants acquire water from the saprolite, they also acquire important metal nutrients from that zone. Moreover, during drier periods, deep-rooted plants acquire more water and nutrients from the saprolite. Because saprolite is a zone of active mineral dissolution, plant uptake of deep water and nutrients could have significant impacts on bedrock weathering, particularly under future drought-prone climates.

Mountainous watersheds of the western United States that provide freshwater to millions of people (1) are warming at a rate of 0.5 to 1.0 °C/decade (2), with more intense drought events predicted (3). Drought and warming have multiple impacts on watershed ecology and water resources including reduced soil moisture and lowered groundwater tables, which causes stress to vegetation and may influence the rate of bedrock weathering (2, 4). Deep root growth is a key adaptive trait in some plants, including trees and woody shrubs, enabling access to water (rock moisture) from soil and bedrock layers that can reach more than 1 m below the ground surface (5–7). Deep-rooted plants can increase ecosystem drought resistance by performing hydraulic uplift from deep soils and groundwater, enabling redistribution to shallow soils (8, 9), and by driving shallow and deep biogeochemical cycling, including an active deep nitrogen cycle (10).

Deep roots may also enable the acquisition of nutrients released from bedrock weathering beneath the soil horizons (11–13). These plant available nutrients are primarily found in the exchangeable pool, that is, the fraction in pore water and absorbed onto the surface of soil particles (14). Evidence for plant acquisition of cations released from weathering bedrock has been provided by the $^{87}Sr/^{86}Sr$ ratio of plant tissue (12, 13, 15). Strontium containing minerals have a characteristic $^{87}Sr/^{86}Sr$ ratio that is typically distinct from local atmospheric sources and not affected by biogeochemical process because it is corrected for mass-dependent fractionation in the measurement process (16). Hence, plant $^{87}Sr/^{86}Sr$ can indicate the source of strontium and other chemically similar cation nutrients, such as Ca and Mg. McCulley et al., demonstrated that deep (>1 m) nutrient uptake occurs in arid and semiarid ecosystems (15). Blum et al., identified the sources of cation nutrients in exchangeable pool and found that mycorrhizal weathering may provide important nutrients for plants (17). Perakis and Pett-Ridge discovered that bedrock sources supplied higher cation nutrients to nitrogen fixing red alder trees than nonfixing tree species (18). In these studies, however, the relationships between water availability and nutrient acquisition by deep roots were not examined.

We measured strontium and water isotopes to identify cation nutrient sources and infer net cation and water acquisition depths for three deep- and one shallow-rooted plant species along a mountainous hillslope transect at a well-characterized field site, the East River watershed, Colorado. We further applied dendrochronological and Sr isotope methods to sagebrush growth rings finding that Sr isotope variations, interpreted to be due to changes in cation acquisition depth, but not growth ring width, show a strong correlation

Author contributions: L.L., J.N.C., and B.G. designed research; L.L., J.N.C., M.B., and W.D. performed research; Y.W., C.B., M.S., B.W.G., S.E.B., B.F., J.S., C.C., A.H., N.J.B., and K.H.W. contributed new reagents/analytic tools; L.L. analyzed data; Y.W. and C.C. compiling rooting depth observations; A.H. assisted field observations; N.J.B. and K.H.W. assisted funding acquisition and field observation; and L.L. and B.G. wrote the paper.

The authors declare no competing interest.

This article is a PNAS Direct Submission.

[1]To whom correspondence may be addressed. Email: bgilbert@lbl.gov.

This article contains supporting information online at https://www.pnas.org/lookup/suppl/doi:10.1073/pnas.2528407123/-/DCSupplemental.

Published March 24, 2026.

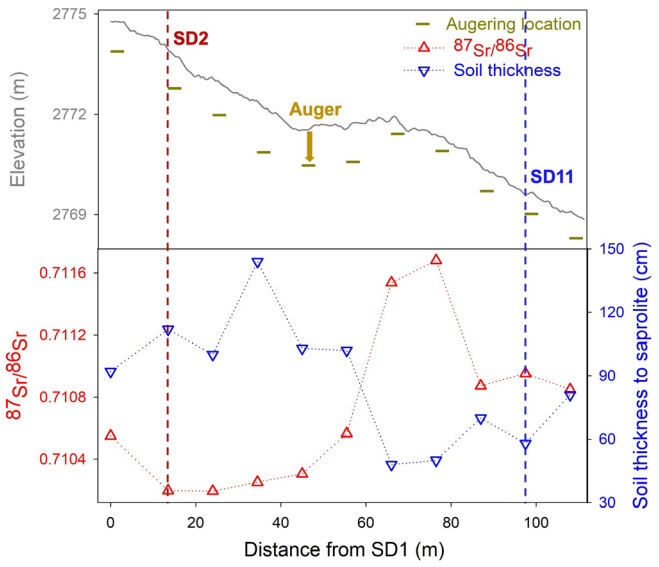

Fig. 1. *Top*: elevation along the sampling transect, and elevation of saprolite–soil transition layer; *Bottom*: $^{87}Sr/^{86}Sr$ ratio of soil exchangeable Sr at depth of 40 to 50 cm, and soil thickness to saprolite at each site along the transect. The green dashed lines mark the locations (SD2 and SD11) of the soil pits and plant study.

with historical precipitation records. This work clarifies the relationship between soil water availability and water and nutrient acquisition and provides insight into predicting deep-rooted plant contributions to silicate weathering in deep soils.

Results

Deep-Rooted Plants Acquire Cations and Water from Deeper Pools. Soil and plant characteristics were studied at 11 locations across the ~110 m transect illustrated in *SI Appendix*, Fig. S1. Soil thickness varied between 40 cm and 140 cm and showed an approximately inverse relationship with the $^{87}Sr/^{86}Sr$ ratio in the exchangeable pool at a depth of 40 to 50 cm (Fig. 1). This depth, below the typical shallow rooting zone (~30 cm), was selected for geochemical analyses to assess potential deep root nutrient sources. Aboveground measurements of plant average canopy dimensions showed a relationship between canopy size and soil depth for sagebrush (*Artemisia Tridentata ssp. vaseyana*) but not lupine (*Lupinus argenteus*) or sunflower (*Helianthus*) (*SI Appendix*, Fig. S2). Transect site SD2 with deeper soil (80 to 90 cm) and site SD11 with shallower soil (40 to 50 cm) were selected for soil pit and plant study. Exposure of the saprolite confirmed that the maximum auger depth coincided with the soil-to-saprolite transition. Plant rooting depths were consistent with a prior biomass sampling effort in the same alpine meadow (*SI Appendix*, Fig. S3) but more delicate tracking of sagebrush and lupine tap and fine roots revealed that they extended through fractures within saprolite to greater depths than previously observed. (*SI Appendix*, Figs. S4 and S5). Soil or saprolite samples were collected for vertical profiles of mineralogy (*SI Appendix*, Fig. S6) and the strontium isotopic composition of the exchangeable pool.

At both sites, the $^{87}Sr/^{86}Sr$ ratio in the exchangeable pool increased with depth from the topsoil into the saprolite (Fig. 2, *Lower*), with a pronounced increase at the soil–saprolite transition. At both sites, the $^{87}Sr/^{86}Sr$ ratio in plant leaf tissues was within belowground values and spanned a significant range (Fig. 2, *Upper*). Grass leaf tissues contained $^{87}Sr/^{86}Sr$ ratios that were very close to the exchangeable pool at 5 cm depth. This is consistent with prior observations that grass litter and tissue $^{87}Sr/^{86}Sr$ ratios are typically very close to the shallow soil exchangeable pool despite significant variation in this ratio over the geographic range of an individual species (18, 19). The deep-rooted plant leaf tissues (sunflower, lupine, and sagebrush) showed higher $^{87}Sr/^{86}Sr$ ratios, indicating that deep-rooted plants access, on average, deeper pools of Sr. The $^{87}Sr/^{86}Sr$ data suggest that sagebrush acquired nutrients from the deepest locations compared to the other deep-rooted plants, with an average depth close to the soil–saprolite transition layer.

The isotopic composition of plant leaf water indicates that deeper-rooted species also utilize a deeper source of water. Plots of δD vs. $\delta^{18}O$ for leaf water from sagebrush, lupine, and sunflower align along lines with divergent slopes (Fig. 3). These differing slopes are consistent with species-specific controls on plant water evaporation, likely regulated by stomatal conductance (20, 21). Because the sampling sites are in close proximity, at similar altitudes, and share comparable landscape positions, differences in relative humidity or boundary layer conductance are unlikely to explain the observed variation among species. The lower intersection of the sagebrush evaporative line with the local meteoric water line (LMWL) and the variations of δ-values of soil water with depth indicate that sagebrush likely relies on a deeper water source than lupine and sunflower. The water content of grass leaf tissue was too low to permit water isotope analysis.

Silicate Weathering Is an Increasing Source of Cations in Deeper Nutrient Pools. The dominant sources of strontium, and their characteristic isotopic ratios, were identified to develop a mixing model to quantify the sources of cations accessed by shallow and deep-rooted plants. Distinct $^{87}Sr/^{86}Sr$ ratios for wet precipitation and dry deposition were found from measurements of monsoon precipitation and atmospheric dust (*SI Appendix*, Table S2). The Sr isotope ratios (~0.71006) and Ca/Sr molar ratios (~550 to 595) of

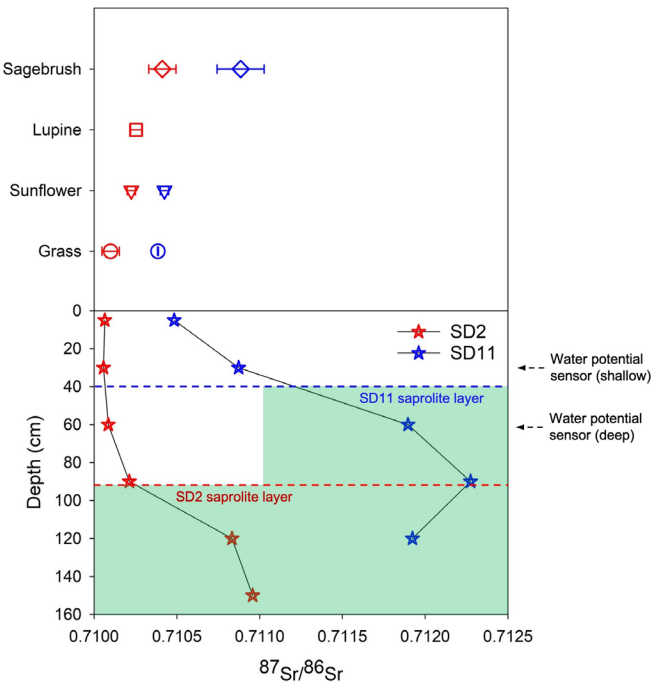

Fig. 2. *Top* panel: $^{87}Sr/^{86}Sr$ ratio for leaves of individual plant species from two sites, including sagebrush, lupine, sunflower, and grass. *Bottom* panel: depth-dependent profile of the $^{87}Sr/^{86}Sr$ ratio in the soil exchangeable pool at these sites. Green shading denotes the saprolite zone with the soil–saprolite transition at 80 to 90 cm (SD2) and 40 to 50 cm (SD11) highlighted with red and blue dashed lines, respectively.

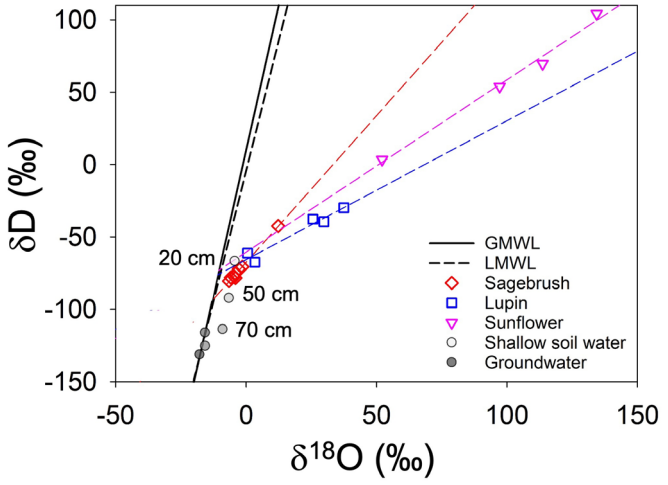

Fig. 3. Relationships between δD and $\delta^{18}O$ of leaf water for different plant species at SD2. GMWL is the global meteoric water line that represents the linear trend of δD and $\delta^{18}O$ for worldwide precipitation, while LMWL represents the linear trend of δD and $\delta^{18}O$ for local precipitation.

the surface soil exchangeable pool are very close to those values of wet deposition and indicate low inputs from dry deposition. The exchangeable radiogenic Sr isotope ratios do not show a strong correlation with Ca/Sr and 1/Sr, indicating that soil Sr derived from more than two sources (*SI Appendix*, Fig. S16). Common strontium bearing minerals in the Mancos shale bedrock are carbonates, apatite, and silicates. Calcite and dolomite were undetectable in the soil profile down to 1.5 to 2 m, however, consistent with the previously reported carbonate weathering front (22), and were excluded (*SI Appendix*, Fig. S7). Although apatite was not detectable in powder X-ray diffraction (XRD) data, the Ca:P ratio from 1 M HNO_3 extraction indicated the presence of a calcium phosphate mineral in all samples (*SI Appendix*, Figs. S6 and S8 and Table S1). Phosphorous K-edge X-ray absorption spectroscopy (XAS) confirmed the presence of fluorapatite reaching ~95% of the phosphate content in the least weathered samples (*SI Appendix*, Fig. S9).

Soil and parent minerals contain several silicate phases known to host divalent cations, including albite, chlorite, and illite. The silicate digestion step liberated high Mg but low Sr concentrations, yet the recovered Sr had a highly radiogenic Sr isotope ratio. XRD following silicate digestion revealed that chamosite and illite are the more easily dissolved silicates that likely provide the major contributions to exchangeable Sr (*SI Appendix*, Fig. S6*B*). The elemental and isotopic compositions of the endmember pools—apatite, silicate minerals, and rainwater—are given in *SI Appendix*, Table S2. The $^{87}Sr/^{86}Sr$ ratios of the soil exchangeable pools lie between 0.71006 and 0.71227, which is higher than rainwater and apatite and significantly lower than the silicates. The increase with depth of the radiogenic Sr isotopes in soil exchangeable pool is therefore primarily driven by inputs from silicate weathering.

A single strontium isotopic ratio cannot apportion contributions from three endmembers and hence the mixing model was expanded to include both $^{87}Sr/^{86}Sr$ and Mg/Sr ratios (*SI Appendix*, Fig. S10). The model calculates that silicate weathering contributed 0.9 to 6.3% of exchangeable Sr, increasing with depth (Fig. 4*A*). Applying the $^{87}Sr/^{86}Sr$ mixing model to the Sr and Mg composition of plant leaf tissues shows that all plants primarily acquired Sr from atmospheric deposition and apatite weathering. Among all plant species, deep-rooted plants showed a higher contribution of Sr from silicate weathering.

Silicate minerals contain a much higher quantity of the nutrients such as Mg and K, relative to apatite or atmospheric inputs (*SI Appendix*, Table S2). By using the Mg/Sr ratio of each end member, the mixing model predicts that 27 to 76% of exchangeable Mg was derived from silicate weathering. Correspondingly, the proportion of plant uptake of silicate-derived Mg increased from 42% in shallow-rooted grass to 58% in sagebrush at SD11. The Ca in both the soil exchangeable pool and plant material was mainly derived from apatite weathering and atmospheric deposition, due to a low content of Ca in silicate minerals (*SI Appendix*, Fig. S11).

Wet Precipitation Regulates the Depth of Sagebrush Nutrient Acquisition. The $^{87}Sr/^{86}Sr$ ratio of bioavailable Sr in soils is generally stable on seasonal to annual timescales (23). Records of Sr isotope ratios preserved in plant tissues, therefore, can be used to track changes in the Sr source (24) and to infer shifts in nutrient acquisition depth. Polished cross sections of the main stem from one sagebrush plant from each of the two study locations revealed growth rings that were used to estimate the plant ages and nutrient

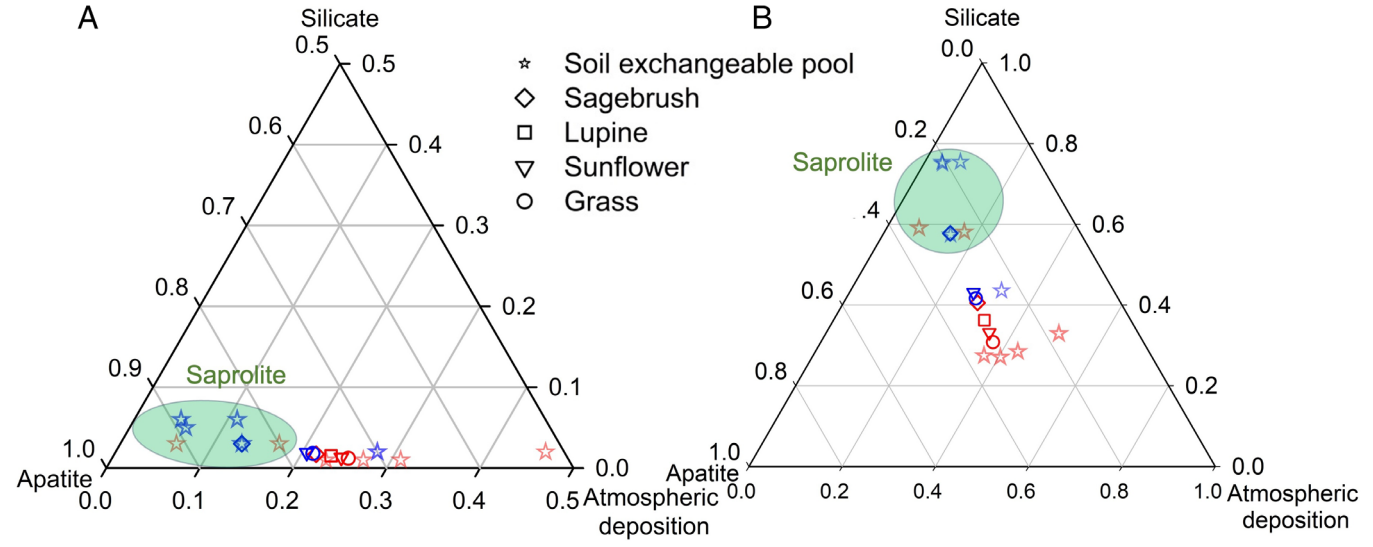

Fig. 4. Proportion of each source (atmospheric deposition, apatite, and silicate weathering) in soil exchangeable pool, individual plant species for Sr (*A*) and Mg (*B*) at location SD2 (red) and SD11 (blue) (see *Materials and Methods* for extraction and model).

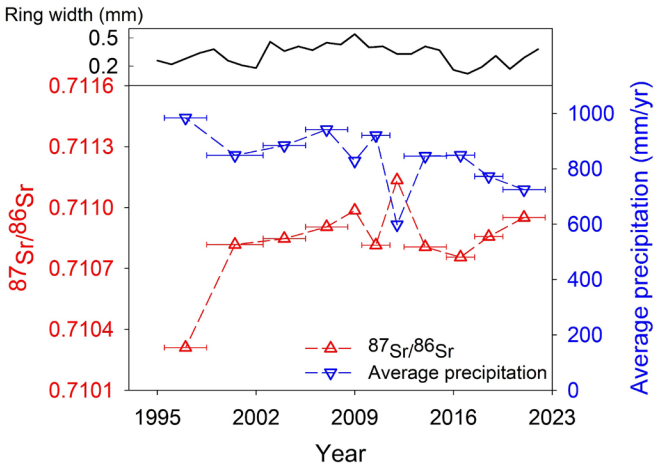

Fig. 5. Comparison of sagebrush growth-ring $^{87}Sr/^{86}Sr$ ratios with annual precipitation and ring-width chronology. *Top* panel: Mean annual ring widths over time. *Bottom* panel: The red curve represents the measured $^{87}Sr/^{86}Sr$ ratios from pooled growth ring samples (details shown *SI Appendix*, Table S3), and the blue curve shows corresponding annual average precipitation for corresponding water years.

depths (photos in *SI Appendix*, Fig. S12). The oldest plant, a ~30-y-old sagebrush, was from site SD11 with the shallowest soil. The dendrochronological ring width did not show evident correlation with the record of water year precipitation at the nearest meteorologic site (*SI Appendix*, Fig. S13*B*). In contrast, the $^{87}Sr/^{86}Sr$ ratios from tissue that was cut from individual growth rings or from 2 to 3 neighboring rings are inversely correlated with the average precipitation during the corresponding years (Fig. 5 and *SI Appendix*, Fig. S13*A*). The large excursion in years 2012 to 2013 coincides with an extended spell of low water availability known as the North American drought (25, 26). Growth ring data from the SD2 sagebrush revealed a similar inverse correlation (*SI Appendix*, Fig. S14*A*), but the younger plant did not experience the North American drought. The proportion of mobile Sr within sectioned growth rings is measured to be only ~5% and hence the tree ring record of Sr isotopes is likely well preserved (*SI Appendix*, Fig. S14*B*). Although acid rain or dust deposition can influence Sr isotope ratios in tree growth rings (27, 28), this was not observed in a nearby study (28).

The growth ring data show that lower precipitation is associated with higher $^{87}Sr/^{86}Sr$ ratios and hence a cation nutrient source that is deeper and with a higher contribution from silicate weathering. Because these data average all nutrient sources, the maximum depths of acquisition are also likely deeper. The inner wood rings inferred to capture the youngest growth in the period 1997 to 2000 show lower $^{87}Sr/^{86}Sr$ values than later rings. This early period is interpreted as a lowering of the mean cation nutrient depth as the sagebrush roots grow downward into the saprolite.

Discussion

Soil Water Availability Drives the Depth of Both Water and Nutrient Acquisition. In alpine and subalpine mountainous watersheds, plants experience annual cycles of wet and dry soil conditions with varying duration and intensity (*cf* soil water potential data, *SI Appendix*, Fig. S15). Dynamic soil water availability, mainly governed by wet precipitation (1), is essential to mobilize nutrients and enable pathways of nutrient acquisition (29, 30). Prior studies have shown that deep-rooted plants can, in dry periods, transport deep soil water to shallow soil (8), and that such hydraulic uplift can enhance soil nitrogen cycling (9), demonstrating that deep water acquisition can drive shallow nutrient cycling and acquisition. This work expands our knowledge of the coupling between water and nutrient acquisition by showing that variation in the main driver of soil water availability can also drive plants to acquire both water and cation nutrients from deeper saprolite or bedrock regions (Figs. 2 and 3). This conclusion is further supported by the correlation between sagebrush growth ring strontium isotopic data and the historical precipitation records. Because the depth of water acquisition by woody shrubs and trees is broadly observed to vary in response to water limitation (31, 32), it is likely that the mean depth of water and nutrient acquisition covaries for many deep-rooted plants.

Enhanced Plant Uptake of Bedrock-Derived Cations during Drought. Although atmospheric wet deposition contributes to plant Sr input, macronutrients such as Mg and Ca are primarily derived from bedrock silicate and apatite weathering. We used the mixing model to estimate how changing precipitation affects the proportion of nutrient sources from silicate weathering based on the growth ring $^{87}Sr/^{86}Sr$ data (Fig. 6). Sagebrush acquired up to a ~20% larger proportion of divalent cations such as Mg from silicate minerals during drier years than during wetter years. An annual precipitation of ~770 mm/y is likely the threshold governing whether sagebrush, on average, acquires nutrients from deeper soil (30 to 60 cm) or from shallow soil (0 to 30 cm). Other ecosystems, particularly those that developed on igneous rock, have been shown to have more intense bedrock silicate weathering and likely will have more plant uptake of silicate-derived cation nutrients than observed in the present ecosystem on shale (33, 34).

The three-decade dendrochronology captured a steadily decreasing trend in precipitation that is associated with an increasing trend in cation uptake from deep soil to bedrock. Such drought-driven enhancement of plant acquisition of water and nutrients from greater depth could increase mineral dissolution rates via different mechanisms. For example, the pH of the rhizosphere is lowered by cation uptake, coupled to proton release to maintain cell electroneutrality, and by microbial respiration generating CO_2, stimulated by organic exudation (36, 37). Cation uptake could also lower the pore water mineral saturation state. Relationships between nutrient acquisition, deep rhizosphere biogeochemistry, and mineral dissolution rates, however, are complex (38, 39) and will require further study and modeling (40). Nevertheless, through these mechanisms, deep-rooted plants could intensify bedrock weathering in response to surface

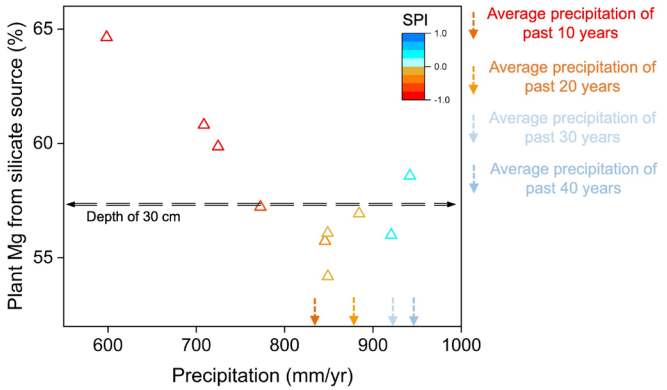

Fig. 6. Ratio of predicted sagebrush Mg from silicate sources vs. precipitation. These plot markers are colored by standard precipitation index (SPI) values, which are used to indicate wet (positive SPI) or drought conditions (negative SPI) (35). The vertical dashed arrows indicate the average precipitation of the last four decades at the sampling site with same color scheme.

water limitation. In contrast, abiotic chemical weathering is much more likely to be limited by lower transport rates under drought (41). Deeper nutrient acquisition may also pose greater phytotoxic threat to deep-rooted plants and associated communities because potentially toxic metals release from parent rock weathering (42). Hence, the global trend of more frequent and intense drought events may modify plant physiological responses, accelerate contribution of nutrient uplift by deep-rooted plants, and enhance plants' contribution to bedrock weathering thus river solute concentrations (2).

Materials and Methods

Sampling Site and Transect. The study site is a ~110-m-long transect in an alpine meadow on the north-facing hillslope in the upper East River watershed, underlain by Mancos Shale (*SI Appendix*, Fig. S1). The climate at this area is continental subarctic with mean annual temperature −14 ± 3 °C and mean annual precipitation of 823 mm/y over past 10 y. On the hillslope, mixed plant species composition is perennial bunchgrass (e.g., *Festuca arizonica*), forbs (e.g., *Lupinus spp., Veratrum californicum,* and *Potentilla gracillis*), and shrub (*Artemisia tridentata*). The weathering of bedrock strongly influenced the water chemistry of solute export of the East River water to Colorado River (43). The transect was selected and studied in July 2023. The transect runs approximately perpendicular to suite of boreholes installed in 2018 (22, 44) and lies above the Pumphouse site where East River water has been sampled since 2014 (45). The transect followed a compass direction of ~140° at approximately constant elevation (2,772 ± 3 m), running parallel with the East River and perpendicular to the dominant slope. The transect traversed regions with variable densities of the main deep-rooted plant species at this altitude, big sagebrush, lupine, sunflower, as well as shallow-rooted needlegrass. Soil water potential meters were installed at 25 cm and 60 cm during a subsequent field trip and recorded shallower and deeper saturation before, during, and after the water year 2025.

Sample Collection and Analysis. The sampling campaign was conducted in June–July 2023 (monthly temperature: 14.0 ± 2 °C). The soil thickness was determined by coring to as deep as the hand-auger could be advanced. Two sites (SD2 and SD11, Fig. 1) were selected for further sampling and analysis. Four plant species, including big sagebrush, lupine, sunflower, and needlegrass were mixed along the transect. The average canopy dimensions of individual plant were based on the estimated diameter of a spheroid equal to the volume of each plant (calculated by measured length, width, and height) (46, 47). Along the transect (Fig. 1), leaf tissues from all four species (n = 3 to 4 for each plant species) within a 1-m radius of each auger hole were collected in falcon tubes sealed with parafilm. Associated soil samples at SD2 and SD11 (every 30 cm from surface to saprolite at 150 cm) were also collected in falcon tubes with parafilm and immediately stored in cooler. Rain water samples were collected in August–September 2023 and 2024 close to the sampling location. Dust samples were also collected using passive sampling collector with 3 M HNO_3 prewashed quartz fiber filter (pore size 1.0 μm). All water samples (both of rain water and river water samples) were filtered to 0.22 μm and subsequently acidified to pH of ~2 with high-purity concentrated HNO_3.

Bulk soil and saprolite samples were sieved through a 2 mm mesh and ground into powder using a mortar and pestle for geochemical analysis and XRD. Geochemical analyses were performed for major elements quantification at the laboratory of ALS Global (Reno, NV). The major elements (SiO_2, Fe_2O_3, Al_2O_3, CaO, MgO, Na_2O, K_2O, Cr_2O_3, TiO_2, MnO, P_2O_5, SrO, and BaO) were analyzed following the method ME-ICP06. XRD was performed on a laboratory diffractometer (Rigaku SmartLab) and analyzed using the Profex software (48).

To assess the elemental profile, and the relative changes in concentration to other elements in rock, the mass transfer coefficient (τ) was calculated following equation (49):

$$\tau_{i,j} = \frac{C_{j,w}C_{i,p}}{C_{j,p}C_{i,w}} - 1,$$

where $C_{j,w}$ and $C_{j,p}$ represent the concentration of element j in the weathered and parent samples, and, $C_{i,w}$ and $C_{i,p}$ indicate the concentration of immobile element i in the weathered and parent samples, respectively. Ti was used as the immobile element as previous study because Ti is resistant to chemical weathering (22). The positive value of $\tau_{i,j}$ indicate the enrichment of j, and negative value indicate depletion of j, with respect to the parent samples (samples at ~12 m were used).

Soil moisture and leaf water content were measured by vacuum-extracting nearly all water contents to liquid nitrogen from fresh soil and leaves. The water isotopes of soils and leaf tissues were then measured using an Off-Axis Integrated Cavity Output Spectrometer coupled with an autosampler interfaced with a heated injector block (Los Gatos Research, San Jose) at the Center for Isotope Geochemistry at Lawrence Berkeley National Lab. Subsamples of soil were ground to fine powder using an agate ball mill for elemental analysis.

To separate the source of nutrients, the dried soil samples were extracted sequentially. The exchangeable pool (digest 1) was extracted using 1 g of soil mixed and shaken for 2 h with 10 ml of unbuffered 1 M NH_4Ac extractant. The apatite pool was extracted using residue of exchangeable extraction, shaken with 1 M HNO_3 overnight at room temperature (digest 2). The dominant silicate pool was extracted using 1.5 M HNO_3 at 120 °C overnight as digest 3.

Plant leaves were rinsed twice with 0.1 M HNO_3 to remove any dust from the leaf surface. The rinsed solutions have low Sr concentrations (110 ng/g leaves) and similar $^{87}Sr/^{86}Sr$ ratio to leaf tissues (with average Sr concentration of 13,250 ± 3,459 ng/g), which indicates minimal contribution from dust deposition. Subsamples of ground plant leaf powder were being burned to ashes using muffle furnace at 450 °C for 8 h, with a rate of 30 to 40 °C/h of ramping up temperature. The plant ashes were then dissolved in 1 M HNO_3 several times until all ash minerals were being dissolved. Solutions were then combined and filter through 0.22 μm polyethersulfone (PES) membrane and acidified to 2% ultrapure HNO_3 before further analysis. The cation concentrations and DOC (dissolved organic carbon) in all solutions were measured using inductively coupled plasma mass spectrometry (ICP-MS, Elan DRC II, PerkinElemer SCIEX, USA) and TOC-VCPH (Shimadzu Corporation, Japan), respectively.

The extracted solutions of soil exchangeable pool were aliquoted into Teflon vials and evaporated for Sr purification. The dried aliquots were treated with concentrated nitric acid at 120 °C to breakdown organic matter. Then, 200 ng of Sr were purified with 8 N HNO_3 and collected with deionized (DI) water using Teflon columns filled with Sr resin (Eichrom Technologies). The purified Sr was taken up into 2% phosphoric acid and dried on Re filaments with a $TaCl_5$ emitter solution. $^{87}Sr/^{86}Sr$ was measured using a Triton multicollector thermal ionization mass spectrometry (TIMS, Thermo Fisher) at the Center for Isotope Geochemistry at Lawrence Berkeley National Lab. During the analysis, the average $^{87}Sr/^{86}Sr$ of NBS 987 (Sr isotopic standard) was 0.710260 ± 9 (±2 s external; $n = 10$).

The $^{87}Sr/^{86}Sr$ of the apatite pool was determined by digestion step 2 of the saprolite samples. The $^{87}Sr/^{86}Sr$ of silicate was determined by the average $^{87}Sr/^{86}Sr$ of digestion step 3. The $^{87}Sr/^{86}Sr$ from atmospheric deposition was determined by using the average value of $^{87}Sr/^{86}Sr$ of rain water.

Strontium Isotope Mixing Calculations. Based on end-members mixing equations (16), the Sr isotopic composition δ_{mix} of a three-components mixture in soil exchangeable pool is

$$\delta_{mix} = \frac{M_1^{Sr}\delta_1 + M_2^{Sr}\delta_2 + M_3^{Sr}\delta_3}{M_1^{Sr} + M_2^{Sr} + M_3^{Sr}}, \quad [1]$$

where M_n^{Sr} represents the mass of Sr in component n, δ_n is $^{87}Sr/^{86}Sr$ in compoent n.

For the fraction of Sr in a mixture from component 1 (f_1, that represents to proportion of Sr from atmospheric deposition):

$$f_1 = \frac{M_1^{Sr}}{M_1^{Sr} + M_2^{Sr} + M_3^{Sr}},$$

while

$$f_1 + f_2 + f_3 = 1. \quad [2]$$

To derive each f to Eq. **1**

$$f_1\delta_1 + f_2\delta_2 + f_3\delta_3 = \delta_{mix}. \quad [3]$$

To estimate Mg budget in mineral dissolution and solution mixing using Sr as the Mg proxy:

$$f_1 M_{mix}^{Sr}\left(\frac{Mg}{Sr}\right)_1 + f_2 M_{mix}^{Sr}\left(\frac{Mg}{Sr}\right)_2 + f_3 M_{mix}^{Sr}\left(\frac{Mg}{Sr}\right)_3 = M_{mix}^{Mg},$$

where $(Mg/Sr)_n$ represents the molar ratio of Mg/Sr in each endmember/source n either from mineral weathering or atmospheric deposition), and $(Mg/Sr)_{mix}$ represents the molar ratio of Mg/Sr in soil exchangeable pool. The equation was simplified as:

$$f_1\left(\frac{Mg}{Sr}\right)_1 + f_2\left(\frac{Mg}{Sr}\right)_2 + f_3\left(\frac{Mg}{Sr}\right)_3 = \left(\frac{Mg}{Sr}\right)_{mix}. \quad [4]$$

Based on Eqs. **2**–**4**, a ternary plot in a Cartesian plane with δ and Mg/Sr axes was created to determine the fraction (*SI Appendix*, Fig. S10). The fraction of Sr in the exchangeable pool from each source can be determined and expressed from the ternary plot and the normalized ternary plot.

Extensive studies of both Sr isotope and geochemical analysis indicated that plants primarily take up cation nutrients from soil exchangeable pool (12, 17, 19, 34). Due to plant preferential acquisition of cation nutrient (Mg, and Ca) than Sr (12, 50), here we use the source of exchangeable Sr which has the identical Sr isotope ratio to plants, to represent the source of Sr in plant tissues. Because of the significant linear relationship between exchangeable Mg/Sr_{molar} and $^{87}Sr/^{86}Sr$ among all soil samples, the plant Sr source can thus be determined by the same methods as exchangeable Sr (*SI Appendix*, Figs. S16 and S17). Tracing Mg dynamics with Sr isotopes requires inference of Sr fraction with Mg/Sr_{molar} of each source:

$$f_1^{Mg} = \frac{f_1\left(\frac{Mg}{Sr}\right)_1}{f_1\left(\frac{Mg}{Sr}\right)_1 + f_2\left(\frac{Mg}{Sr}\right)_2 + f_3\left(\frac{Mg}{Sr}\right)_3}, \quad [5]$$

where f_1^{Mg} is the fraction of Mg from atmospheric deposition, f_1 is the fraction of Sr from atmospheric deposition, $(Mg/Sr)_1$ is the molar ratio of Mg to Sr from atmospheric deposition.

X-ray Tomography. During a biomass sampling campaign at this site, sagebrush and lupine taproots were observed to grow into fractured shale saprolite at a depth of approximately 1 m. In an attempt to trace root distributions in saprolite, roughly cylindrical saprolite blocks of diameter ~30 cm and height ~50 cm containing one root were exposed and embedded in a two-component epoxy for transport and X-ray tomography. The blocks were surrounded by aluminum metal sheet and approximately 5 cm cement was poured at the base and hardened overnight. The epoxy was mixed and filled the remaining space for the aluminum shell to the top of the saprolite block.

The excess epoxy was cut away from around the location of the root using a commercial blade saw followed by a 5-inch coring bit (UKAM Industry). The trimmed root and saprolite sample were scanned on a GE Lightspeed 16 medical computed tomography (CT) scanner. Each CT scan was performed at 120 kV and 160 mA, at voxel size of 400 × 400 × 625 μm^3. Initial image processing and analysis were conducted using ImageJ–a public domain JAVA-based software (51). Subsequent 3D segmentation was performed using Dragonfly. Regions of rock, fracture, and root were visually labeled to train the on-the-fly thresholding algorithm. Although the rendered lupin data confirm that the taproot penetrates the saprolite, the root was indistinguishable from fractures after ~10 cm. The tomographic study did not provide insight into root-fracture distributions and was not repeated for the sagebrush study.

Historical Annual Net Precipitation. The monthly time series of precipitation from 1996 to 2023 was downloaded from PRISM Group (Parameter-elevation Regression on Independent Slopes Model), Northwest Alliance for Computational Science and Operation at the Oregon State University. The total precipitation each water year was calculated by summing up monthly precipitation data from Oct 1st to Sept 30th of the following year.

Soil Apatite Determination. The phosphorus K-edge XAS was conducted on beamline 14-3 at Stanford Synchrotron Radiation Lightsource (SSRL, Stanford, CA). The powdered soil and rock samples were loaded onto mylar tape in a thin and homogeneous layer. The spectra were collected in fluorescence mode using a Vortex detector under a helium atmosphere at room temperature. The energy was selected using a water-cooled double-crystal Si (111) monochromator, with 1 mm vertical slits and 2.5 mm horizontal slits. Calibration of a monochromator was performed based on the energy of the first pre-edge feature of PPh_4-Br (2146.96 eV). Spectra of fluorapatite (Sigma Aldrich), hydroxyapatite (Sigma Aldrich), calcium phosphate dibasic (Sigma Aldrich), and sagebrush root tissue powder were collected as standard references. References of phosphate absorbed onto iron and clay minerals that were collected in a previous study were also used for data fitting (52).

The background of each XAS spectra was subtracted by linear fitting the pre-edge region (2,115 to 2,145 eV). The spectra were then normalized by a second-order polynomial to the postedge region (2,175 to 2,250 eV) with the setting edge jump E_0 (2,165 eV). The proportion of phosphorus species in soil was estimated using least-squares linear combination fits in Athena.

Growth Ring Separation and Sr Immobility Test. The dendrochronology records of the sagebrush growth ring are determined following standard dendrochronology procedures (53). The growth ring sample were mounted, sanded, and measured ring width using a sliding scale micrometer (Velmex Inc., Bloomfield, NY) with Acu-Rite encoder (Heidenhain 178 Corp., Shaumberg, IL). Although distinct ring bands were small, combined 2 to 3 growth-rings were separated manually (*SI Appendix*, Table S3). The Sr concentration and isotopic analysis of each separated samples were determined following the same protocol as leaf treatment in Sample analysis.

The mobile Sr for each growth ring was extracted with 20 mM KCl as an analog to flowing sap (54). The mixture of growth ring samples with KCl solution was shaken for 2 d after 5 min sonication. The ~5% mobile Sr for each growth ring indicates a negligible effect of Sr interring mobility.

Statistical Analyses. Statistical analyses were performed using Systat 13. The relationship between canopy dimension with soil thickness was evaluated using weighted linear regression with significance set at $P < 0.05$. Results of strontium isotope mixing model were calculated in R version 4.5.1.

Data, Materials, and Software Availability. Source data are available in the ESS-DIVE repository at DOI: 10.15485/2998779 (55).

ACKNOWLEDGMENTS. This work was supported by the Watershed Function Scientific Focus Area at Lawrence Berkeley National Laboratory funded by the US Department of Energy, Office of Science, Biological and Environmental Research under Contract No. DE-AC02−05CH11231. We thank Jade J. Basinski, and Dr. Annaleise R. Klein from the Aristilde research group at Northwestern University for sharing X-ray absorption spectroscopy spectra of standard references. We acknowledge Jillian Banfield, Donald Depaolo, and William Dietrich for their suggestions and feedback to this work. Use of the Stanford Synchrotron Radiation Lightsource, SLAC National Accelerator Laboratory, is supported by the U.S. Department of Energy, Office of Science, Office of Basic Energy Sciences under Contract No. DE-AC02-76SF00515. The SSRL Structural Molecular Biology Program is supported by the DOE Office of Biological and Environmental Research, and by the NIH, National Institute of General Medical Sciences (P30GM133894).

Author affiliations: [a]Department of Earth and Planetary Science, University of California, Berkeley, CA 94720; [b]Earth and Environmental Science Area, Lawrence Berkeley National Laboratory, Berkeley, CA 94720; [c]Rocky Mountain Biological Laboratory, Crested Butte, CO 81224; [d]Department of Forestry and Environmental Resources, North Carolina State University, Raleigh, NC 27695; [e]Department of Geosciences, Stony Brook University, Stony Brook, NY 11794; [f]Stanford Synchrotron Radiation Lightsource, SLAC National Accelerator Laboratory, Menlo Park, CA 94025; [g]Department of Environmental Science, Policy and Management, University of California, Berkeley, CA 94720; and [h]Department of Biological and Ecological Engineering, Oregon State University, Corvallis, OR 97331

1. R. C. Bales *et al.*, Mountain hydrology of the western United States. *Water Resour. Res.* **42**, 2005WR004387 (2006).
2. W. Zhi *et al.*, Significant stream chemistry response to temperature variations in a high-elevation mountain watershed. *Commun. Earth Environ.* **1**, 43 (2020).
3. E. R. Siirila-Woodburn *et al.*, A low-to-no snow future and its impacts on water resources in the western United States. *Nat. Rev. Earth Environ.* **2**, 800–819 (2021).
4. C. N. Dahm, M. A. Baker, D. I. Moore, J. R. Thibault, Coupled biogeochemical and hydrological responses of streams and rivers to drought. *Freshw. Biol.* **48**, 1219–1231 (2003).
5. A. Odone, O. Popovic, K. Thorup-Kristensen, Deep roots: Implications for nitrogen uptake and drought tolerance among winter wheat cultivars. *Plant Soil* **500**, 13–32 (2024).
6. L. H. Comas, S. R. Becker, V. V. Cruz, P. F. Byrne, D. A. Dierig, Root traits contributing to plant productivity under drought. *Front. Plant Sci.* **4**, 442 (2013).

7. A. Darrouzet-Nardi, C. M. D'Antonio, T. E. Dawson, Depth of water acquisition by invading shrubs and resident herbs in a Sierra Nevada meadow. *Plant Soil* **285**, 31–43 (2006).
8. J. H. Richards, M. M. Caldwell, Hydraulic lift: Substantial nocturnal water transport between soil layers by Artemisia tridentata roots. *Oecologia* **73**, 486–489 (1987).
9. Z. G. Cardon, J. M. Stark, P. M. Herron, J. A. Rasmussen, Sagebrush carrying out hydraulic lift enhances surface soil nitrogen cycling and nitrogen uptake into inflorescences. *Proc. Natl. Acad. Sci U.S.A.* **110**, 18988–18993 (2013).
10. K. L. Crutchfield-Peters, D. M. Rempe, A. K. Tune, T. E. Dawson, Linked nitrogen and carbon dynamics reveal distinct pools and patterns in a deep, weathered bedrock rhizosphere. *Proc. Natl. Acad. Sci U.S.A.* **122**, e2400452122 (2025).
11. J.-L. Maeght, B. Rewald, A. Pierret, How to study deep roots–and why it matters. *Front. Plant Sci.* **4**, 299 (2013).
12. R. A. Oeser, F. Blanckenburg, Strontium isotopes trace biological activity in the Critical Zone along a climate and vegetation gradient. *Chem. Geol.* **558**, 119861 (2020).
13. D. Uhlig, W. Amelung, F. Von Blanckenburg, Mineral nutrients sourced in deep regolith sustain long-term nutrition of mountainous temperate forest ecosystems. *Global Biogeochem. Cycles* **34**, e2019GB006513 (2020).
14. E. K. Miller, J. D. Blum, A. J. Friedland, Determination of soil exchangeable-cation loss and weathering rates using Sr isotopes. *Nature* **362**, 438–441 (1993).
15. R. McCulley, E. Jobbágy, W. Pockman, R. Jackson, Nutrient uptake as a contributing explanation for deep rooting in arid and semi-arid ecosystems. *Oecologia* **141**, 620–628 (2004).
16. R. C. Capo, B. W. Stewart, O. A. Chadwick, Strontium isotopes as tracers of ecosystem processes: Theory and methods. *Geoderma* **82**, 197–225 (1998).
17. J. D. Blum *et al.*, Mycorrhizal weathering of apatite as an important calcium source in base-poor forest ecosystems. *Nature* **417**, 729–731 (2002).
18. S. S. Perakis, J. C. Pett-Ridge, Nitrogen-fixing red alder trees tap rock-derived nutrients. *Proc. Natl. Acad. Sci U.S.A.* **116**, 5009–5014 (2019).
19. B.-Y. Song, J.-S. Ryu, H. S. Shin, K.-S. Lee, Determination of the source of bioavailable Sr using $^{87}Sr/^{86}Sr$ tracers: A case study of hot pepper and rice. *J. Agric. Food Chem.* **62**, 9232–9238 (2014).
20. L. Zhan, J. Chen, L. Li, P. Xin, Plant water use strategies indicated by isotopic signatures of leaf water: Observations in southern and northern China. *Agric. For. Meteorol.* **276**, 107624 (2019).
21. L. A. Cernusak *et al.*, Stable isotopes in leaf water of terrestrial plants. *Plant Cell Environ.* **39**, 1087–1102 (2016).
22. J. Wan *et al.*, Bedrock weathering contributes to subsurface reactive nitrogen and nitrous oxide emissions. *Nat. Geosci.* **14**, 217–224 (2021).
23. J. F. Hogan, J. D. Blum, Tracing hydrologic flow paths in a small forested watershed using variations in 87Sr/86Sr, [Ca]/[Sr], [Ba]/[Sr] and δ18O. *Water Resour. Res.* **39**, 2002WR001856 (2003).
24. R. Alexander Bentley, Strontium isotopes from the Earth to the archaeological skeleton: A review. *J. Archaeol. Method Theory* **13**, 135–187 (2006).
25. J. E. Bell *et al.*, Evaluation of the 2012 drought with a newly established national soil monitoring network. *Vadose Zone J.* **14**, vzj2015.02.0023 (2015).
26. J. T. Overpeck, B. Udall, Climate change and the aridification of North America. *Proc. Natl. Acad. Sci U.S.A.* **117**, 11856–11858 (2020).
27. T. Drouet, J. Herbauts, D. Demaiffe, Long-term records of strontium isotopic composition in tree rings suggest changes in forest calcium sources in the early 20th century. *Global Change Biol.* **11**, 1926–1940 (2005).
28. O. L. Miller, D. K. Solomon, D. P. Fernandez, T. E. Cerling, D. R. Bowling, Evaluating the use of strontium isotopes in tree rings to record the isotopic signal of dust deposited on the Wasatch Mountains. *Appl. Geochem.* **50**, 53–65 (2014).
29. S. A. Barber, *Soil Nutrient Bioavailability: A Mechanistic Approach* (John Wiley & Sons, 1995).
30. P. H. Nye, P. B. Tinker, *Solute Movement in the Soil-Root System* (Studies in Ecology, University of California Press, 1977), vol. 4.
31. T. E. Dawson, J. S. Pate, Seasonal water uptake and movement in root systems of Australian phraeatophytic plants of dimorphic root morphology: A stable isotope investigation. *Oecologia* **107**, 13–20 (1996).
32. S. Kolb, Transport constraints on water use by the Great Basin shrub, Artemisia tridentata. *Plant Cell Environ.* **22**, 925–935 (1999).
33. J. C. Pett-Ridge, L. A. Derry, A. C. Kurtz, Sr isotopes as a tracer of weathering processes and dust inputs in a tropical granitoid watershed, Luquillo Mountains, Puerto Rico. *Geochim. Cosmochim. Acta* **73**, 25–43 (2009).
34. J. Bouchez, F. von Blanckenburg, The role of vegetation in setting strontium stable isotope ratios in the critical zone. *Am. J. Sci.* **321**, 1246–1283 (2021).
35. B. Lloyd-Hughes, M. A. Saunders, A drought climatology for Europe. *Int. J. Climatol.* **22**, 1571–1592 (2002).
36. P. Hinsinger, O. N. F. Barros, M. F. Benedetti, Y. Noack, G. Callot, Plant-induced weathering of a basaltic rock: Experimental evidence. *Geochim. Cosmochim. Acta* **65**, 137–152 (2001).
37. M. Keiluweit *et al.*, Mineral protection of soil carbon counteracted by root exudates. *Nat. Clim. Change* **5**, 588–595 (2015).
38. Q. Fang *et al.*, Mineral weathering is linked to microbial priming in the critical zone. *Nat. Commun.* **14**, 345 (2023).
39. K. Zhalnina *et al.*, Dynamic root exudate chemistry and microbial substrate preferences drive patterns in rhizosphere microbial community assembly. *Nat. Microbiol.* **3**, 470–480 (2018).
40. Z. Li *et al.*, A framework for integrating genomics, microbial traits, and ecosystem biogeochemistry. *Nat. Commun.* **16**, 2186 (2025).
41. K. Maher, The role of fluid residence time and topographic scales in determining chemical fluxes from landscapes. *Earth Planet. Sci. Lett.* **312**, 48–58 (2011).
42. X. Dupla, B. Möller, P. C. Baveye, S. Grand, Potential accumulation of toxic trace elements in soils during enhanced rock weathering. *Eur. J. Soil Sci.* **74**, e13343 (2023).
43. M. J. Winnick *et al.*, Snowmelt controls on concentration-discharge relationships and the balance of oxidative and acid–base weathering fluxes in an alpine catchment, East River, Colorado. *Water Resour. Res.* **53**, 2507–2523 (2017).
44. S. S. Hubbard *et al.*, The East River, Colorado, watershed: A mountainous community testbed for improving predictive understanding of multiscale hydrological–biogeochemical dynamics. *Vadose Zone J.* **17**, 1–25 (2018).
45. K. Williams *et al.*, Anion data for the East River Watershed, Colorado (2014–2023) (Environmental System Science Data Infrastructure for a Virtual Ecosystem, 2024).
46. R. R. Renne *et al.*, Soil and stand structure explain shrub mortality patterns following global change–type drought and extreme precipitation. *Ecology* **100**, e02889 (2019).
47. P. L. Ferguson *et al.*, The effect of mechanical canopy reduction on big sagebrush plant communities. *Ecol. Appl.* **35**, e70056 (2025).
48. N. Doebelin, R. Kleeberg, Profex: A graphical user interface for the Rietveld refinement program BGMN. *Appl. Crystallogr.* **48**, 1573–1580 (2015).
49. G. H. Brimhall, W. E. Dietrich, Constitutive mass balance relations between chemical composition, volume, density, porosity, and strain in metasomatic hydrochemical systems: Results on weathering and pedogenesis. *Geochim. Cosmochim. Acta* **51**, 567–587 (1987).
50. A. A. Dasch *et al.*, The relative uptake of Ca and Sr into tree foliage using a whole-watershed calcium addition. *Biogeochemistry* **80**, 21–41 (2006).
51. C. A. Schneider, W. S. Rasband, K. W. Eliceiri, NIH image to ImageJ: 25 years of image analysis. *Nat. Methods* **9**, 671–675 (2012).
52. J. J. Basinski *et al.*, Unraveling iron oxides as abiotic catalysts of organic phosphorus recycling in soil and sediment matrices. *Nat. Commun.* **15**, 5930 (2024).
53. J. W. Wason, M. Dovciak, C. M. Beier, J. J. Battles, Tree growth is more sensitive than species distributions to recent changes in climate and acidic deposition in the northeastern United States. *J. Appl. Ecol.* **54**, 1648–1657 (2017).
54. G. Kim, J. Lee, Micromachined needle-like calorimetric flow sensor for sap flux density measurement in the xylem of plants. *Sci. Rep.* **14**, 14838 (2024).
55. L. Li *et al.*, Data for "Depth of nutrient uptake by deep-rooted plants is regulated by water availability." Watershed Function SFA, ESS-DIVE repository. https://data.ess-dive.lbl.gov/datasets/doi:10.15485/2998779. Accessed 6 March 2026.